Modeling and control of shape distribution of protein crystal aggregates

Joseph Sang-Il Kwon [a], Michael Nayhouse [a], Panagiotis D. Christofides [a,b], Gerassimos Orkoulas [a,*]

[a] Department of Chemical and Biomolecular Engineering, University of California, Los Angeles, CA 90095, USA
[b] Department of Electrical Engineering, University of California, Los Angeles, CA 90095, USA

AUTHOR-HIGHLIGHTS

- Kinetic Monte Carlo simulation of protein crystal growth.
- Approximate model for evolution of protein crystal shape.
- Model predictive control of protein crystal shape.
- Disturbance handling using model predictive control.

ARTICLE INFO

ABSTRACT

We focus on the modeling and control of protein crystal aggregates in a large-scale batch crystallizer used to produce tetragonal hen-egg-white (HEW) lysozyme crystals. We initially present a kinetic Monte Carlo (kMC) simulation for the modeling of the crystal nucleation, growth, and shear-induced aggregation in an effort to control the evolution of the crystal shape distribution. Through experimental data, the crystal growth rate is calibrated and an empirical expression for the nucleation rate is also developed. Then, the method of moments is applied to a comprehensive population balance model to derive a reduced-order moment model that describes the dynamic evolution of the three leading moments of the crystal volume distribution. Along with mass and energy balances for the continuous phase, the moment model is used to design a model predictive control (MPC) strategy which drives the crystal shape distribution to a desired set-point value through the manipulation of the crystallizer jacket temperature. Compared to conventional operating strategies used in industry, it is demonstrated that the proposed MPC strategy is able to produce crystal aggregates with a desired shape distribution and a low polydispersity effectively dealing with the undesired effects of biased nucleation, depletion in the solute concentration, and changes in the average crystal shape due to the aggregation process.

© 2013 Elsevier Ltd. All rights reserved.

1. Introduction

The biopharmaceutical market is one of the fastest growing areas in the $1 trillion pharmaceutical industry. Within biopharmaceutical production, protein crystallization plays a crucial role. For example, more than 100 therapeutic proteins have been licensed and more proteins are currently under research or development. However, of the 100 therapeutic proteins with production licenses, only a few are being sold in a crystalline form in the market due to significant technological challenges in their production. The main technological challenge in producing protein crystals lies in the complexity of protein crystallization and the presence of nonlinearities in many factors involved in the system. Researchers recently have developed models for protein nucleation (Galkin and Vekilov, 1999; Pusey and Nadarajah, 2002) and crystal growth (Durbin and Feher, 1986; Feher and Kam, 1985; Forsythe et al., 1999; Kurihara et al., 1996), and consequently significant advances have been made in the field of modeling of crystallization processes describing the shape and size distributions of the produced protein crystals. To this end, kinetic Monte Carlo simulation methods, which have been widely used to simulate molecular dynamic processes (Bortz et al., 1975; Dai et al., 2005, 2008; Gillespie, 1976, 2007; Rathinam et al., 2003; Reese et al., 2001; Snyder et al., 2005; Gilmer and Bennema, 1972), have been successfully applied to compute the net crystal steady-state growth rate accounting for the dependence of migration and

detachment rates on the local surface configuration. To implement the kMC methodology over the entire lattice, we extended the methodology of Christofides et al. (2008) to rate equations which were first developed by Durbin and Feher (1991). Additionally, the reader may refer to our previous works for the details of the methodology for single crystal growth (Nayhouse et al., 2013), for a batch of crystals nucleated throughout the run (Kwon et al., 2013), and for a comparative study of an MPC strategy with other conventional operating policies taken into consideration mass and energy balances for the continuous phase (Kwon et al., in press).

In spite of all these advances, mass production of protein crystals has not been achieved yet due to a lack of knowledge on scale-up of protein crystallization to large scale. Although there has been a number of computational and theoretical studies of understanding the shape control of crystals in a variety of small-scale crystallization systems (Liu et al., 2010a; Liang et al., 2013; Wang et al., 2008), no significant advancement has been made associated with the shape control of crystal aggregates in a large-scale batch crystallization system. The crystal aggregation is caused by shear-induced forces from a stirring process which is necessary for a large-scale batch crystallizer in order to maintain the particulate phase in suspension (i.e., to avoid crystal sedimentation) (Schmidt et al., 2005).

One of the main purposes of protein crystallization is to identify the structure of, for example, a therapeutic protein via nuclear magnetic resonance or X-ray crystallography depending on the molecular weight of a specific macromolecular protein (Rosenberger et al., 1996; Vekilov and Chernov, 2003; Wiencek, 1999). This requires preparation of a well-defined protein crystal with a desired morphology, because a low polydispersity is also necessary for a good separation by filtration. In protein crystals, proteins are naturally folded in their most stable form, and are very compact so that only minimal storage space is required. In this regard, a fine protein crystal with a desired shape can be used as a carrier for the delivery of biopharmaceuticals where it has many advantages such as enhanced stability, adjustable solubility, and controllable release.

Therefore, the first aim of the present work focuses on the modeling of aggregation of protein crystals alongside crystal nucleation and growth to investigate the influence of stirring on the size and morphology of crystal aggregates. First of all, we assume that the continuous phase is dilute enough to make only binary aggregation possible. Furthermore, the corresponding turbulent shear rate within the crystallizer is characterized by the average velocity gradient of the flow field. An appropriate aggregation kernel is used to compute the rate at which a binary aggregation occurs, and this rate strongly depends on the crystal sizes and the crystallizer operating parameters (Kusters et al., 1997; Saffman and Turner, 1954). The aggregation for lysozyme crystals with a diameter approximately in the range of 1–50 μm is mainly induced by shear forces according to the Kolmogorov microscale analysis (Kusters et al., 1997). Lastly, an aggregate will be formed as two crystals completely merge along with their internal coordinates resulting in a decrease in the total number of crystals and an increase in the average crystal size. For the purpose of simulation, it is assumed that the shapes of bigger crystals are maintained for the aggregate after the aggregation process. Extensive simulation studies are carried out to evaluate the influence of aggregation on the shape and size distributions of the crystals at the end of the batch run.

The second aim of the current work focuses on the simulation and control of protein crystal aggregation along with its crystallization. We initially present a population balance model for the process which accounts for simultaneous nucleation, crystal growth, and shear-induced aggregation. The high-dimensionality of population balance model, however, leads to a complicated

controller design, which cannot be readily implemented in practice (Chiu and Christofides, 1999). To circumvent these problems, the method of moments is used to derive the moment model that describes the dynamic evolution of the three leading moments of crystal volume distribution in a crystallizer (Kalani and Christofides, 2002). The moment model is closed according to the fact that crystal volume can be properly approximated by a lognormal distribution. Along with a nonlinear algebraic equation that describes the dependence of crystal growth rates on temperature and protein solute concentration, and the energy and mass balance models that describe the changes of the temperature in the crystallizer and the solute concentration in the continuous phase, the moment model is employed to design a model predictive controller (MPC). The proposed model predictive control scheme is used to regulate the average shape of crystal aggregates to a desired set-point value with a low polydispersity.

Another contribution of this work is to examine the performance of a model predictive controller (MPC) in comparison with constant supersaturation control (CSC) and constant temperature control (CTC).

2. Crystallization process description and modeling

2.1. Crystal nucleation

In our previous work (Kwon et al., in press), we assume that HEW lysozyme nucleus is a cube with infinitesimal size (i.e., $V=0$) (Nanev and Tsekova, 2000; Suzuki et al., 1994). The supersaturation σ is defined as $\sigma = \ln(c/s)$, where c (mg/mL) is the protein solute concentration and s (mg/mL) is the solubility. The protein solubility depends on temperature (°C) and is expressed through the following third-order polynomial at pH 4.5 and 4% (w/v) NaCl (Cacioppo et al., 1991; Cacioppo and Pusey, 1991):

$$s(T) = 2.88 \times 10^{-4} T^3 - 1.65 \times 10^{-3} T^2 + 4.62 \times 10^{-2} T + 6.01 \times 10^{-1}. \tag{1}$$

The nucleation rate, $B(T,c)$, at pH 4.5 and 4% (w/v) NaCl is taken from (Galkin and Vekilov, 2001):

$$B(T,c) = \begin{cases} 0.041\sigma + 0.063 & \text{for} \quad \sigma \geq 3.11 \\ 8.0 \times 10^{-8} \exp(4.725\sigma) & \text{for} \quad \sigma < 3.11 \end{cases} \tag{2}$$

with units $(\text{cm}^{-3}\text{s}^{-1})$.

2.2. Crystal growth

We model the 3-D crystal growth with two representative faces (i.e., (110) and (101) directions) via kMC simulations. The interested readers may refer to our earlier work (Nayhouse et al., 2013; Kwon et al., 2013, in press) for further details regarding the kMC methodology. The following rate expressions adopted from Durbin and Feher (1991) and Ke et al. (1998) are used to simulate the kinetics of crystal surface.

Attachment rate:

$$r_a = K_0^+ \exp\frac{\Delta\mu}{k_B T}, \tag{3}$$

where K_0^+ is the attachment coefficient, k_B is the Boltzmann constant, T is the temperature (K), and $\Delta\mu = k_B T\sigma$.

Detachment rate:

$$r_d(i) = K_0^+ \exp\left(\frac{\phi}{k_B T} - i\frac{E_{pb}}{k_B T}\right), \tag{4}$$

Migration rate:

$$r_m(i) = K_0^+ \exp\left(\frac{\phi}{k_B T} - i\frac{E_{pb}}{k_B T} + \frac{E_{pb}}{2k_B T}\right), \tag{5}$$

where E_{pb} is the average binding energy per bond, ϕ is the total binding energy per molecule of a fully occupied lattice, and i is the number of nearest neighbors.

2.3. Crystal aggregation

2.3.1. General considerations

Aggregation processes result in a decrease in the total number of particles and an increase in the average particle size. The shear force induced by agitation, which is required in the scale-up of a particulate process, plays a key role in the aggregation maintaining the particulate phase in suspension. Aggregation has an important influence on the quality of particulate products, especially for dense particles such as protein crystals, and should be taken into consideration in the modeling of large-scale crystallization processes. This work is a comprehensive attempt to model the batch particulate process including nucleation, crystal growth, and aggregation in a stirred batch process, so that the design of the batch crystallizer and the subsequent scale-up process can be carried out in a more quantitative way. In this context, it is necessary to find key kinetic expressions for aggregation that enables us to quantify the major factors including aggregation efficiency and frequency.

The aggregation process can be divided into two steps. First, particles must be transported into a very small neighborhood of one another, accounted as collision frequency and collision efficiency. A simple idea is that an aggregate will be formed if an aggregate is sufficiently stable that it can overcome the repulsive forces such as hydrodynamic drag and the viscous fluid layer between those particles undergoing aggregation. More specifically, there are several aggregation types. Brownian motion induced aggregations are the prevailing mechanism for submicrometer particles. Particles whose sizes are in the range of 1–50 μm are mostly under the influence of shear forces, and this mechanism dominates in particulate processes. Although it is not of particular interest in this work, crystals with a size greater than 50 μm are controlled by differential sedimentation or inertia (Cheng et al., 2009).

2.3.2. Maximum local energy dissipation rate ε_{max}

In the works by Smejkal et al. (2013) and Hollander et al. (2003), it is shown that crystallization experiments at higher stirrer speeds show a reduced formation of crystal aggregates which is favorable in the subsequent separation process by filtration. Although higher stirrer speeds are preferred in order to achieve more crystals with uniform size and shape, it is apparent that there is a physical limitation on the stirrer speed that is achievable by a motor. Therefore, it is important to identify a maximum local energy dissipation rate (ε_{max}), which measures the hydromechanical stress resulted from agitation and is related to the highest impeller speed for the batch crystallizer. This energy is usually converted into heat, but leads to a negligible temperature change. For a given input power level, P, we can calculate the corresponding mass related mean power input, $\bar{\varepsilon}$, for a batch crystallizer as follows (Smejkal et al., 2013):

$$\bar{\varepsilon} = \frac{P}{\rho V_{batch}} = \frac{\omega M_{torque}}{\rho V_{batch}} = \frac{2\pi n M_{torque}}{\rho V_{batch}} \tag{6}$$

where ρ is the density of the continuous phase in the stirred tank and V_{batch} is the volume of the batch crystallizer. Additionally, the mean power input, $\bar{\varepsilon}$, by stirring in a tank was determined by measuring the torque, M_{torque}, at the agitator shaft at a specific stirrer speed, n. The ratio of the maximum local energy dissipation, ε_{max}, which depends on the geometrical parameters of reactor and stirrer type, and the mass related impeller power, $\bar{\varepsilon}$, was determined by the following equation (Henzler, 2000):

$$\frac{\varepsilon_{max}}{\bar{\varepsilon}} \approx \frac{a}{(d/D)^2(h/d)^{2/3}z^{0.6}(\sin\theta)^{1.15}z_I^{2/3}(H/D)^{-2/3}} \tag{7}$$

The details about geometry of the batch crystallizer and the stirrer type are taken from Smejkal et al. (2013): unbaffled vessel ($a=16$); diameter of the impeller ($d=0.06$ m); inner tank diameter ($D=0.12$ m); height of the impeller blade ($h=0.04$ m); tank filling height ($H=0.12$ m); number of impeller blades ($z=3$); blade inclination to the horizontal ($\theta=40°$); and number of impellers ($z_I=1$). Under this specification, it is computed that $\varepsilon_{max}/\bar{\varepsilon}=72$.

2.3.3. Shear rate G_{shear}

In particular, when the optimum mean power input is $\bar{\varepsilon}=30$ mW/kg, the corresponding maximum energy dissipation ($\varepsilon_{max}=2.16$ W/kg) is determined by Eq. (7). Different stirrer speeds ranging from 50 to 300 rpm are considered. This range of stirrer speed is taken from the experimental work by Smejkal et al. (2013) where the aggregation of crystals is studied and the crystal growth condition in the work is similar to that of our simulation. The turbulent shear rate within the stirred tank, G_{shear}, was characterized by the average velocity gradient of the flow field as is shown in the following expression by Camp and Stein (1943):

$$G_{shear} = \left(\frac{\varepsilon}{\nu}\right)^{0.5} \tag{8}$$

where the kinematic viscosity is $\nu=2.3\times10^{-6}$ cm^2/s, the initial solute concentration is $c=47$ mg/mL, and the shear rate computed by Eq. (8) is $G_{shear}=970$/s.

2.3.4. Kolmogorov microscale η

The Kolmogorov microscale, η, has been used to indicate the length scale of the smallest eddies in turbulent solid–liquid systems and it is related to the local energy dissipation rate, ε, and kinematic viscosity, ν, as follows (Kusters et al., 1997):

$$\eta = \left(\frac{\nu^3}{\varepsilon}\right)^{1/4} \tag{9}$$

In this study, the corresponding Kolmogorov microscale amounts to 48.7 μm when the optimum mean power input and the corresponding maximum energy dissipation are $\bar{\varepsilon}=30$ mW/kg and $\varepsilon_{max}=2.16$ W/kg, respectively.

2.3.5. Collision frequency β_{ij}

For particles and aggregates smaller than the Kolmogorov microscale, collisions induced by the shear force dominates those caused by viscous forces (Kusters et al., 1997). The aggregation kernel, $\beta(V_i, V_j)$, represents the rate at which particles of the volumes V_i and V_j aggregate induced by the shear force and is as follows:

$$\beta_{ij} = \beta(V_i, V_j) = \psi G_{shear}(V_i^{1/3} + V_j^{1/3})^3 \tag{10}$$

where ψ is a constant that depends on the type of flow. For example, ψ is 4/3 for the laminar flow, and (Saffman and Turner, 1954) derived $\psi=1.29$ for the turbulent flow. Additionally, Ilievski and Livk (2006) state that this expression for collision frequency is available up to particles with a diameter of 5–10 times the Kolmogorov microscale.

2.3.6. Mass fractal dimension d_f

Assume for the moment that the aggregate is a solid particle without any empty inner space and its density is identical to that

of the protein crystals. For the purpose of simulation focusing on the shape evolution of crystals, we assume that there are only binary collisions and the shape of a crystal aggregate after collision follows that of the bigger crystal when the binary aggregation occurs. Then, the mass $M(h_{110}, h_{101})$, which is a function of a set of 2 internal coordinates into (110) and (101) directions, of the aggregate enclosed within a small neighborhood from a suitably chosen center is given by

$$M(h_{110}, h_{101}) = \frac{4}{3}\rho h_{110}^2 h_{101} \tag{11}$$

where the characteristic crystal lengths are simply h_{110} and h_{101} as they are presented in Fig. 2. In general, if we were to account for the fact that the region enclosed within the sphere of radius R is not completely filled with particles but contains empty spaces, then the actual mass will be less than that given by Eq. (11). In fact, it turns out that in many cases, one can write

$$M(R) \propto k_a R^{d_f} \tag{12}$$

where d_f is the mass fractal dimension and it is usually less than 3 due to the porosity in aggregates, k_a is the shape factor (e.g., it is $\frac{4}{3}\rho\pi$ for a sphere), and R is the characteristic length. The interested readers may refer to Jiang and Logan (1991) for further analysis on the mass and fractal dimension. In aggregation, the total volume and shape are maintained identical, but the total number of crystals is reduced by one after each aggregation event. Suppose that there are two crystals where the volume of crystal 1 is greater than that of crystal 2, and we denote the dimension of each crystal for (110) and (101) faces as $(h_{110,1}, h_{101,1})$ and $(h_{110,2}, h_{101,2})$, respectively. Therefore, we note that the volume of each crystal can be expressed in terms of crystal shape factor, $\alpha_1 = h_{110,1}/h_{101,1}$ and $\alpha_2 = h_{110,2}/h_{101,2}$, as follows:

$$V_1 = h_{110,1}^2 h_{101,1} = \frac{h_{110,1}^3}{\alpha_1}, \quad V_2 = h_{110,2}^2 h_{101,2} = \frac{h_{110,2}^3}{\alpha_2}$$

As mentioned previously, the crystal shape after the aggregation, α_{agg}, remains identical to that of the bigger crystal (i.e., $\alpha_{agg} = \alpha_1$ since $V_1 > V_2$). Then, the final crystal height in both faces after aggregation can be computed by the following balance equation based on the equation of total volumes before and after the aggregation:

$$h_{110,1}^2 h_{101,1} + h_{110,2}^2 h_{101,2} = \frac{h_{110,agg}^3}{\alpha_{agg}}$$

where $h_{110,agg}$ and $h_{101,agg}$ are the crystal height of the new aggregate for (110) and (101) faces, respectively. Therefore, we can eventually compute $h_{110,agg}$ and $h_{101,agg}$ in the following way:

$$h_{110,agg} = \alpha_{agg}^{1/3}(h_{110,1}^2 h_{101,1} + h_{110,2}^2 h_{101,2})^{1/3}$$

and

$$h_{101,agg} = \left(\frac{h_{110,1}^2 h_{101,1} + h_{110,2}^2 h_{101,2}}{\alpha_{agg}^2}\right)^{1/3}$$

The physical properties and other operating parameters of the particulate process are presented in Table 1.

Table 1
Process parameters for aggregation.

ψ	A constant depending on the type of flow	1.29
G_{shear}	Shear rate	970 1/s
$\bar{\varepsilon}$	Effective mean power input	0.03 m²/s³
ε_{max}	Maximum local energy dissipation rate	2.16 m²/s³
ν	Kinematic viscosity	2.3×10^{-6} m²/s
μ	Dynamic viscosity	0.0024 kg/m s
A_H	Hamaker constant	10^{-19} J

2.3.7. Collision efficiency α_{ij}

In a stirred crystallizer, the aggregates of crystals are compact because they are subject to strong shear flow, and thus the collision efficiency corresponding to the impermeable aggregate is modeled by Vanni and Baldi (2002). The collision efficiency α_{ij}, which is defined as the ratio of the number of collisions to the number of collisions that result in aggregation (i.e., the actual aggregation rate to the theoretical aggregation rate), is then computed by the following equation (Wang et al., 2005):

$$\alpha_{ij} = 0.43 Fl^{-0.18} \quad \text{where } 10 < Fl < 10^5 \tag{13}$$

where Fl is the flow number computed by Balakin et al. (2012) as follows:

$$Fl = \frac{6\pi\mu(V_i^{1/3} + V_j^{1/3})^3 G_{shear}}{8A_H}$$

Fl can be understood as the ratio between the repulsive shear force and the attractive van der Waals force. The coefficient 0.43 in Eq. (13) was obtained by Wang et al. (2005). The Hamaker constant A_H indicates the extent of Van der Waals interaction, and the value is approximately between 10^{-20} and 10^{-19} J for solid–liquid systems. In this study, the value of 10^{-19} J is chosen for A_H. Therefore, by Eqs. (10) and (13), we can conclude that increasing the shear rate increases the relative velocity (i.e., the average velocity gradient) among the particles, and hence the collision frequency is enhanced. However, the efficiency of collisions decreases to zero with further increase in the shear rate. This is because higher shear rates result in stronger hydrodynamic forces acting against the formation of aggregates and thus aggregates are not formed since they do not have sufficient time for the formation of the bond for aggregates. Since the aggregation rate is determined by the product of the collision frequency and the efficiency, shear rate has two conflicting effects on the aggregation. We can compute the Kolmogorov time scale, $(\nu/\varepsilon)^{0.5}$, which indicates how much time is needed for the collision to be successful. With the system parameters described in Table 1, it is calculated that the Kolmogorov time scale is 10^{-4} s. This time scale can be considered to be sufficiently small so that crystal aggregation occurs successfully with the current mean power input, $\bar{\varepsilon} = 30$ mW/kg.

2.3.8. Total collision rate N_{ij}

Let N_{ij} be the total number of collisions occurring per unit time per unit volume between the two classes where each class represents a set of particles with volume V_i and V_j. The shape of lysozyme protein crystals is assumed to be a rectangular prism, and aggregations are treated as binary hard sphere collisions. The number of aggregations occurring during sampling time Δ can be written in terms of aggregation kernel $\beta(V_i, V_j)$, batch reactor volume V_{batch}, collision efficiency α_{ij}, and concentrations of particles of volume V_i and V_j as follows:

$$N_{ij} = \alpha_{ij}\beta(V_i, V_j)m_i m_j V\Delta, \quad 1 \leq i, j \leq C_{total} \tag{14}$$

where m_i is the number concentration (i.e., the number of particles of class i per unit volume). The number C_{total} denotes the total number of classes. In the case of a discrete volume, the rate of formation of particles of size k from the collision of particles of volume i and j is $\frac{1}{2}\sum_{i+j=k} N_{ij}$, where the notation $i+j=k$ indicates that the summation is over all the different combinations of collisions for which

$$V_i + V_j = V_k$$

A factor of 1/2 is introduced because each collision is counted twice in the summation.

In order to execute an aggregation event between two lysozyme crystals in the simulation, first the binary collision probability must be
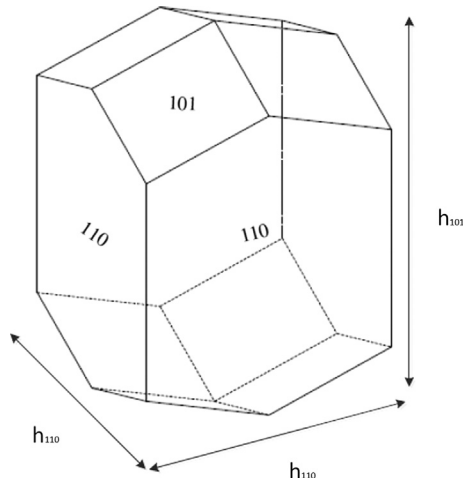
Fig. 1. The geometry model for lysozyme crystal used in the present work.

Table 2
Parameters for the batch crystallizer.

ρ_c	Crystal density	1400 mg/cm³
ΔH_c	Enthalpy of crystallization	−44.5 kJ/kg
ρ	Continuous phase solution density	1047 mg/cm³
C_p	Specific heat capacity	4.13 kJ/K kg
V	Crystallizer volume	5 L
A_j	Surface area of crystallizer wall	0.25 m²
U_j	Heat transfer coefficient of crystallizer wall	1800 kJ/m² h K

calculated according to Eq. (14). For the purposes of the batch crystallization simulation, aggregation events are considered every 0.5 s. By doing this we can take Eq. (14), multiply by 0.5 s and the reactor volume to get the total number of collisions during this time period between the two classes. We use this as a probability of whether an aggregation event happens between the crystal classes *i* and *j*. Then, a random number from [0, 1) is generated, and the aggregation event is executed when the random number is less than the calculated probability. This process has been done over all the crystal classes, and continues throughout the entire batch crystallization simulation.

2.4. Mass and energy balances for the continuous phase

2.4.1. Mass balance

The mass balance in the present work is modeled by assuming that the geometry of lysozyme crystal is a rectangular prism as shown in Fig. 1, and the shape of lysozyme crystal is approximated by a ratio of crystal heights into (110) and (101) directions. The amount of the protein solute removed from the continuous phase due to the crystallization can be computed through the following form:

$$\Delta c(t) = -\frac{\Delta V_c(t)\rho_c N_c(t)}{V_{batch}}, \tag{15}$$

where V_{batch} is the volume of the continuous phase (assuming that the change in V_{batch} is negligible), $\Delta V_c(t)$ is the total volume changes of the entire crystal population, $N_c(t)$ is the number of crystals in batch at time t, ρ_c is the crystal density, and $\Delta c(t)$ is the change of the protein solute concentration in the continuous phase. For the derivation of Eq. (15), the reader may refer to Kwon et al. (in press).

2.4.2. Energy balance

Similarly, the energy balance of the batch crystallization process is shown below:

$$\frac{dT}{dt} = -\frac{\rho_c \Delta H_c}{\rho C_p}\left(\frac{1}{V}\Delta V_c(t)\right) - \frac{U_j A_j}{\rho C_p V}(T - T_j) \tag{16}$$

where T is the crystallizer temperature and T_j is the temperature of the jacket. For the derivation of Eq. (16), the reader may refer to Kwon et al. (in press). The crystallizer parameter values are given in Table 2.

3. Population balance modeling

3.1. Population balance model (PBM) of crystal volume distributions

In this section, we present a population balance model (PBM) for the lysozyme crystallization process accounting for simultaneous nucleation, crystal growth, and aggregation. The evolution of the crystal volume distribution in the batch crystallizer can be obtained from the following partial integro-differential equation:

$$\frac{\partial n(V,t)}{\partial t} + \frac{dV}{dt}\frac{\partial n(V,t)}{\partial V} = \underbrace{\delta(V-V_0)B(T,c)}_{Birth\ by\ nucleation}$$

$$+ \underbrace{\frac{1}{2}\int_0^V \alpha_{eff}\beta(V-\overline{V},\overline{V})n(V-\overline{V})n(\overline{V})\,d\overline{V}}_{Birth\ by\ aggregation}$$

$$- \underbrace{n(V)\int_0^\infty \alpha_{eff}\beta(V,\overline{V})n(\overline{V})\,d\overline{V}}_{Death\ by\ aggregation} \tag{17}$$

where V and $V-\overline{V}$ denote the crystal volumes, t is the time, $n(V,t)$ denotes the lysozyme crystal distribution with volume V, α_{eff} is a constant aggregation efficiency, $\beta(V-\overline{V},\overline{V})$ is the aggregation rate between the crystals with volumes V and $V-\overline{V}$, $\delta(V)$ is the standard Dirac function, and $B(T,c)$ is the nucleation rate. As is obtained from Kwon et al. (in press), dV/dt, which will be denoted as G_{volume} from now on, can be computed by simply measuring the amount of solute concentration drop:

$$G_{volume} = \frac{dV}{dt} \approx -\frac{1}{\Delta t}\left(\frac{V_{batch}\Delta c(t)}{\rho_c N_c(t)}\right), \tag{18}$$

where the right hand side is readily available from Eq. (15).

Then, we can write Eq. (17) along with the boundary condition, which is derived in Appendix A, as follows:

$$\frac{\partial n(V,t)}{\partial t} + G_{volume}\frac{\partial n(V,t)}{\partial V} = \frac{1}{2}\int_0^V \alpha_{agg}\beta(V-\overline{V},\overline{V})n(V-\overline{V})n(\overline{V})\,d\overline{V}$$

$$- n(V)\int_0^\infty \alpha_{eff}\beta(V,\overline{V})n(\overline{V})\,d\overline{V} \tag{19}$$

$$n(0,t) = \frac{B(T,c)}{G_{volume}}$$

3.2. Lognormal volume distribution and moment model

Due to the complexity of the population balance model, it is not directly applicable for numerical computation of the size distribution in real-time, as well as for the design of model predictive controllers that can be readily implemented in practice. In order to circumvent these problems, the method of moments is applied to Eq. (17) for the construction of a low-order ordinary differential equation (ODE) model that accurately reproduces the dominant dynamics of the particulate process. More specifically, the constructed low-order ODEs are used to describe the evolution of the three leading moments of the crystal volume distribution in the turbulent shear regime in a 5 L batch crystallizer. Then, under

the assumption that the changes in the collision efficiency are negligible, we construct a framework for the moment models that describes aggregation mechanisms over the entire batch. These moment models provide acceptable simplification of the population balance equation by modeling the key behavior of the crystal growth, nucleation, and aggregation in the continuous phase. First of all, it is shown in Fig. 3 that the lysozyme crystal volume distribution obtained from kMC simulations can be appropriately characterized by the following lognormal function:

$$n(V,t) = \frac{1}{3\sqrt{2\pi}\ln\overline{\sigma}}\exp\left(-\frac{\ln^2\left(\frac{V}{V_g}\right)}{18\ln^2\overline{\sigma}}\right)\frac{1}{V} \tag{20}$$

where $V_g = M_1^2/(M_0^{3/2}M_2^{1/2})$ is the average crystal volume and $\overline{\sigma}$ is the standard deviation of the crystal volume distribution which is expressed as $\ln^2\overline{\sigma} = \frac{1}{9}\ln(M_0M_2/M_1^2)$. Then, we apply the method of moments to Eq. (17) to compute the approximate models that describe the evolution of the three leading moments of the volume distribution. For this purpose, we defined the jth moment model of the crystal volume distribution as follows:

$$M_j = \int_o^\infty V^j n(V,t)\,dV \tag{21}$$

Furthermore, the moment models of the system can be closed according to the assumption above that the volume distribution follows that of lognormal, and thus an arbitrary moment, M_k, is computed as follows:

$$M_k = M_0 V_g^k \exp\left(\frac{9}{2}k^2\ln^2\overline{\sigma}\right)$$

For further details of the derivation of moment models, the reader may refer to Appendix B. The equations given below describe the three leading moment models for $j = 0, 1, 2$.

Zeroth moment:

$$\frac{dM_0}{dt} = B(T,c) - \alpha_{eff}(M_0M_1 + 3M_{1/3}M_{2/3}) \tag{22}$$

where α_{eff} is the collision efficiency described in Eq. (13) and $B(T,c)$ is justified by the boundary condition in Eq. (19).

First moment:

$$\frac{dM_1}{dt} = G_{volume}M_0 \tag{23}$$

Second moment:

$$\frac{dM_2}{dt} = 2G_{volume}M_1 + 2\alpha_{eff}(M_1M_2 + 3M_{4/3}M_{5/3}) \tag{24}$$

In a nutshell, by putting all these together we can complete the moment models as follows:

$$G_{volume} \approx -\frac{1}{\Delta t}\left(\frac{V_{batch}\Delta c(t)}{\rho_c M_0}\right)$$

$$\frac{dM_0}{dt} = B(T,c) - \alpha_{eff}(M_0M_1 + 3M_{1/3}M_{2/3})$$

$$\frac{dM_1}{dt} = G_{volume}M_0$$

$$\frac{dM_2}{dt} = 2G_{volume}M_1 + 2\alpha_{eff}(M_1M_2 + 3M_{4/3}M_{5/3})$$

$$\frac{dT}{dt} = -\frac{\rho_c\Delta H_c}{\rho C_p}\left(\frac{1}{V}\sum_{i=1}^{N_c(t)}\Delta V_{c,i}\right) - \frac{U_cA_c}{\rho C_p V}(T - T_{j,i})$$

$$\Delta c(t) = -\frac{\rho_c}{V}\sum_{i=1}^{N_c(t)}\Delta V_{c,i}$$

$$M_k = M_0 V_g^k \exp\left(\frac{9}{2}k^2\ln^2\overline{\sigma}\right) \quad \text{for } k = \left(\frac{1}{3},\frac{2}{3},\frac{4}{3},\frac{5}{3}\right)$$

$$V_g = \frac{M_1^2}{M_0^{3/2}M_2^{1/2}}$$

$$\ln^2\overline{\sigma} = \frac{1}{9}\ln\left(\frac{M_0M_2}{M_1^2}\right) \tag{25}$$

Although an aggregation kernel with a constant collision efficiency was considered to deal with the closure issue of the moment models, the model can be further improved by using a nonconstant collision efficiency.

3.3. Relation between crystal volume and shape distributions

In the moment model, we can accurately estimate M_0, which represents the number of crystals in the system, and it is highly coupled with other moments as is shown in Eqs. (23) and (24). Due to the nonlinearity in this problem, we should carefully connect M_0 to the shape distribution, $\alpha = h_{110}/h_{101}$. In the model predictive controller (see Eq. (29)), the average height of the (110) face, $\langle h_{110}(t)\rangle$, at time t is estimated at every sampling time through the following equation:

$$\langle h_{110}(t)\rangle = \frac{\langle h_{110}(t-\Delta)\rangle M_0(t-\Delta)}{M_0(t)} + G_{110}(t-\Delta)\Delta \tag{26}$$

where $G_{110}(t)$ is the growth rate for (110) face, and in the same manner the average height of the crystal face 101, $\langle h_{101}(t)\rangle$, can be computed as follows:

$$\langle h_{101}(t)\rangle = \frac{\langle h_{101}(t-\Delta)\rangle M_0(t-\Delta)}{M_0(t)} + G_{101}(t-\Delta)\Delta \tag{27}$$

where $G_{101}(t)$ is the growth rate for (101) face. By the above equations we can approximate the average crystal shape in the following way:

$$\langle\alpha\rangle \approx \frac{\langle h_{110}(t)\rangle}{\langle h_{101}(t)\rangle} \tag{28}$$

4. Open-loop simulation results

Executing multiple kMC simulations with an infinite number of lattice sites can be considered to be similar to solve Eq. (17) directly (Fichthorn and Weinberg, 1991; Müller-Krumbhaar and Binder, 1973). In this work, we assume that the number of lattice sites used in the kMC simulation is sufficiently high, because no size effects are observed in the systems with more lattice sites (Ke et al., 1998).

In Fig. 2, crystal growth at pH 4.5 and 4% (w/v) NaCl has been properly modeled through a procedure described in the previous work (Nayhouse et al., 2013; Kwon et al. 2013, in press), and plotted against the experimental results at 3.5% and 5.0% NaCl from Durbin and Feher (1986). In particular, $(\phi/k_B, E_{pb}/k_B)_{110} = (1077.26K, 227.10K)$ and $(\phi/k_B, E_{pb}/k_B)_{101} = (800.66K, 241.65K)$ are used to calibrate the simulation results with experimental data for (110) and (101) faces, respectively. Additionally, $K_o^+ = 0.211$ s^{-1}. Then, a set of 3-D plots (cf. Fig. 4) are made from the open-loop simulation results along the set of parameters used in the kMC simulation. The plots represent the algebraic equations linking the temperature and solute concentration dependencies of the steady-state crystal growth rates for (110) and (101) faces and crystal growth rate ratio.

One of the major contributions of this paper is focused on the development of the aggregation process along with nucleation and crystal growth in the kMC simulation. In addition to the growth conditions including temperature, protein solute concentrations, pH, and salt (Aldabaibeh et al., 2009; Weber et al., 2008; Müller et al., 2011; Müller and Ulrich, 2011), as is shown in the previous sections, there are many factors that affect the aggregation rate as

is described by Eqs. (6)–(14). Additionally, the evolution of aggregation along with the nucleation and crystal growth is estimated by using the moment models described in Eq. (25). To verify the accuracy of the moment models, an open-loop simulation is run. Then, the evolution of the number of crystals (M_0), the average crystal shape, and the temperature and solute concentration in the kMC simulation and the moment model are plotted together in Fig. 3. The solute concentration remains almost constant at 47 mg/mL. As is
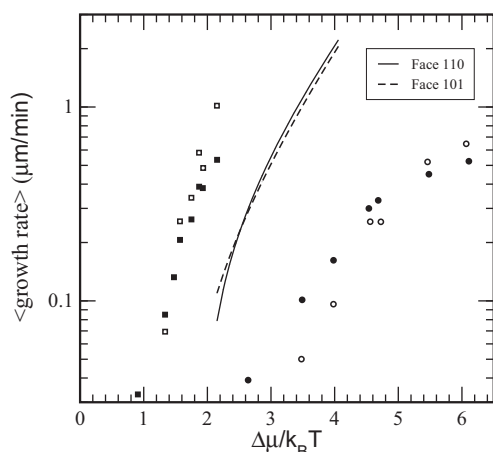
Fig. 2. Growth rates vs. the degree of supersaturation at $c=45$ mg/mL and 4% NaCl. The solid and dashed lines show the growth rates for the kMC model on the (110) and (101) faces, respectively. Experimental data from Durbin and Feher (1986) is also shown at pH=4.6 where the (■) and (□) represent the 101 and 110 faces with 5% NaCl and the (●)/(○) represent the 101 and 110 faces with 3.5% NaCl, respectively.

seen in Eq. (13), the collision efficiency decreases as the crystal sizes increase, because crystals are less likely to adhere to one another due to a short contact time which is undesirable for the aggregation to occur (i.e., a large crystal is more influenced by shear flow).

In this work, however, a constant aggregation efficiency is used to deal with the closure issue in the moment models, and it results in a minor mismatch in M_0 between the moment models and kMC simulations as is shown in Fig. 3. This happens because the constant aggregation efficiency is not able to capture the size-dependent nature of the aggregation. Regardless of the discrepancy in M_0 between the moment models and kMC simulations, the procedure proposed in Eqs. (26)–(28) successfully estimates the average crystal shape distribution based on the growth rates for (110) and (101) faces and the number of crystals in the crystallizer.

Eventually, the development of the moment models guides us in the next section to design a new controller in order to provide optimality as well as robustness in regulating the batch process.

5. Model predictive control of size and shape of crystal aggregates

In the batch crystallization simulation, the role of aggregation events becomes significant in a scaled-up crystallizer as crystal size and the number of crystals increase. Then, the moment model is considered in the controller design in order to predict the system dynamics with a set of low-order ordinary differential equations. The rate of the nucleation and the crystal growth is determined by a set of the crystallizer temperature and solute concentration. However, the shear rate, which is determined by
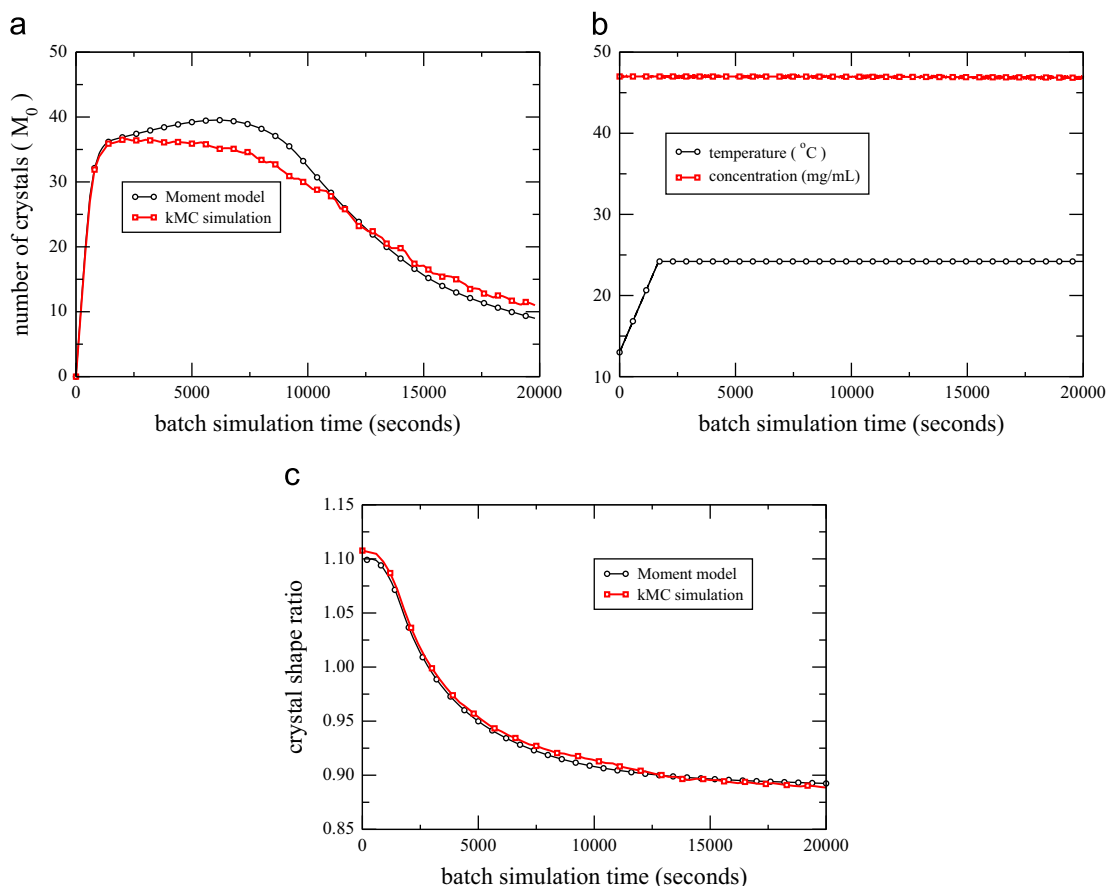

Fig. 3. .Profiles of the open-loop evolution of number of crystals, temperature, protein solute concentration, and crystal shape for tetragonal lysozyme protein crystals at pH 4.5. (a) Number of crystals (M_0). (b) Temperature and concentration. (c) Crystal shape (α).

the stirrer speed (i.e., the only controllable variable in the aggregation rate), is fixed throughout the entire batch run.

In addition to the non-linear models described in Fig. 4(a)–(c), and mass and energy balances introduced in Eqs. (15) and (16), moment models, which account for the number of crystals (M_0), and the average volume (M_1) in the crystallizer, play a key role in estimating the evolution of the crystal volume and shape distributions (Eqs. (26)–(28)). Then, a model predictive controller is designed using only the manipulation of the jacket temperature to produce the crystals with a desired shape and size. Conventional operating strategies may be used, however, there are some issues. For example, due to a lower limit on the temperature, the supersaturation level cannot be maintained to a set-point value when the depletion in the solute concentration is significant.

5.1. Model predictive control formulation

In this work, we consider the control of crystal aggregates along with the moment models and the balance equations by using a model predictive control (MPC) design. Minimizing the deviation of the average crystal shape, $\langle \alpha \rangle$, from a set-point value is chosen as the control objective. The jacket temperature is chosen as a manipulated input, and only the measurements of the solute concentration and the crystallizer temperature are required, assuming other factors remain constant.

The mass and energy balance equations (Eqs. (15) and (16)) and the moment model (Eq. (25)) are considered along with other practical constraints in the control formulation. First, a constraint on the crystallizer temperature is imposed, $4\,^\circ\mathrm{C} \leq T_j \leq 25\,^\circ\mathrm{C}$. Next, $R_T = 2.0\,^\circ\mathrm{C/min}$ is a constraint which will control the maximum

rate of change for the jacket temperature. The cost function penalizes the deviation of the average crystal shape, $\langle \alpha \rangle$, from a set-point value. The proposed MPC formulation is as follows:

$$\underset{T_{j,1},\ldots,T_{j,i},\ldots,T_{j,p}}{\text{minimize}} \sum_{i=1}^{p} F_{\langle \alpha \rangle,i}$$

$$\text{subject to} \quad F_{\langle \alpha \rangle,i} = (\langle \alpha \rangle - \alpha_{\text{set}})^2$$

$$G_i = f_r(T, C, t_i) \quad G_j(t_i) = f_j(T, C, t_i)$$

$$4\,^\circ\mathrm{C} \leq T_j \leq 25\,^\circ\mathrm{C} \quad \left| \frac{T_{j,i+1} - T_{j,i}}{\Delta} \right| \leq 2.0\,^\circ\mathrm{C/min}$$

$$\frac{dT}{dt} = -\frac{\rho_c \Delta H_c}{\rho C_p} \left(\frac{1}{V} \sum_{i=1}^{N_c(t)} \Delta V_{c,i} \right) - \frac{U_c A_c}{\rho C_p V}(T - T_{j,i})$$

$$\Delta c(t) = -\frac{\rho_c}{V} \sum_{i=1}^{N_c(t)} \Delta V_{c,i}$$

$$\langle h_j(t_i) \rangle = \frac{\langle h_j(t_{i-1}) \rangle M_0(t_{i-1})}{M_0(t_i)} + G_j(t_{i-1}) \Delta$$

$$\frac{dM_0}{dt} = B(T, c) - \alpha_{\text{eff}}(M_0 M_1 + 3M_{1/3} M_{2/3})$$

$$\frac{dM_1}{dt} = G_{\text{volume}} M_0$$

$$\frac{dM_2}{dt} = 2G_{\text{volume}} M_1 + 2\alpha_{\text{eff}}(M_1 M_2 + 3M_{4/3} M_{5/3})$$

$$M_k = M_0 V_g^k \exp\left(\frac{9}{2} k^2 \ln^2 \bar{\sigma} \right) \quad \text{for } k = \left(\frac{1}{3}, \frac{2}{3}, \frac{4}{3}, \frac{5}{3} \right)$$

$$V_g = \frac{M_1^2}{M_0^{3/2} M_2^{1/2}}$$

$$\ln^2 \bar{\sigma} = \frac{1}{9} \ln\left(\frac{M_0 M_2}{M_1^2} \right)$$
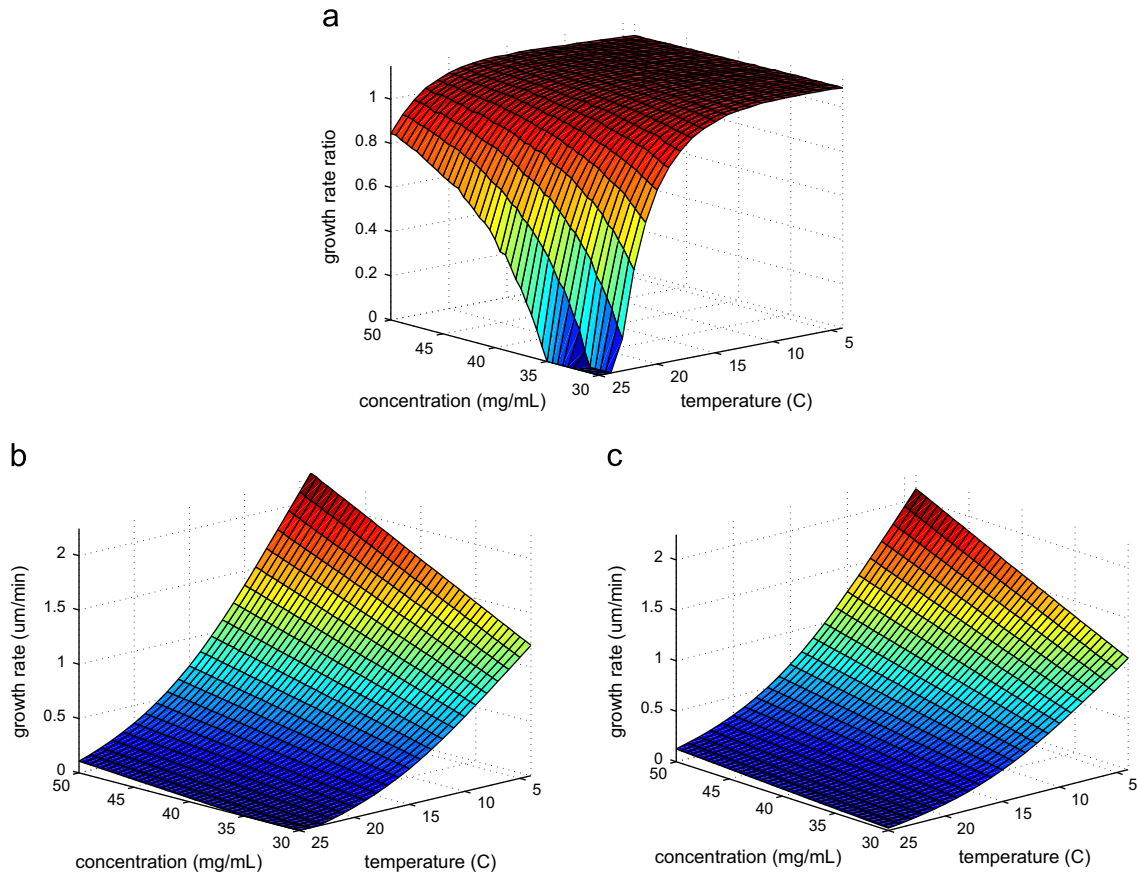

Fig. 4. Profiles for (a) the growth rate ratio between the (110) and (101) faces, and the growth rates for the (b) (110) and (c) (101) faces, respectively, over a protein concentration range from 30 to 50 mg/mL and a temperature range of 4–25 °C. Each point on the three plots is generated by running the kMC simulation under open-loop conditions at pH 4.5. (a) Growth rate ratio. (b) Growth rate of the (110) face. (c) Growth rate of the (101) face.
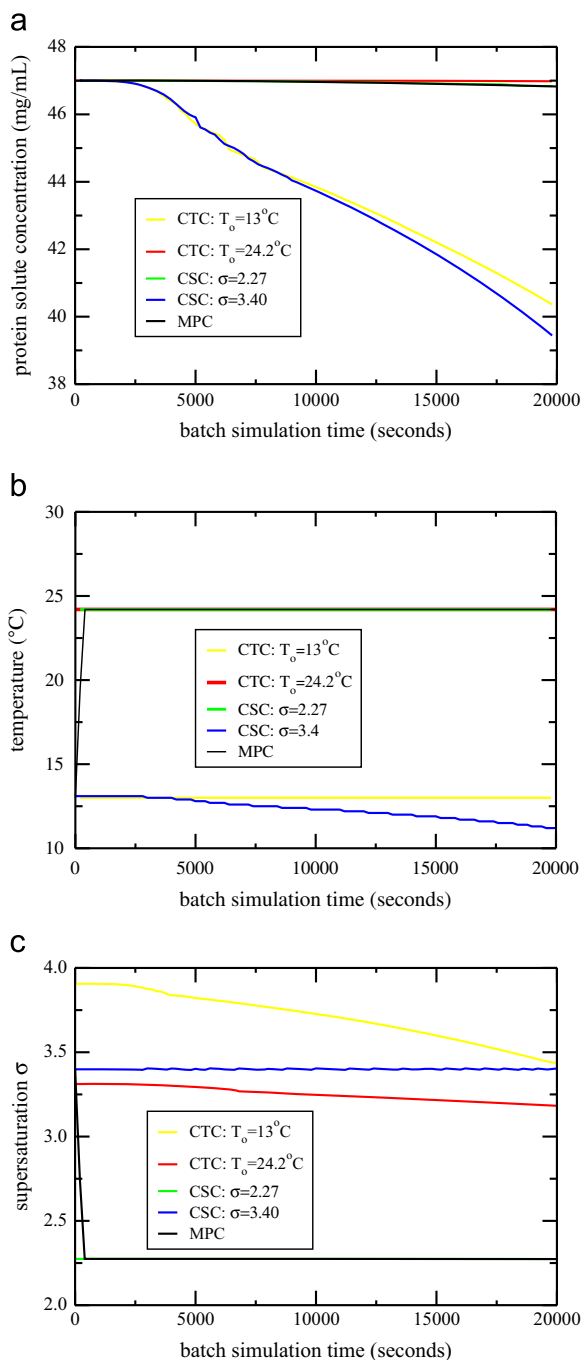
Fig. 5. Profiles of protein solute concentration, crystallizer temperature, and supersaturation vs. time under closed-loop MPC operation during the batch run. The growth rate ratio set-point value is set at $\langle \alpha \rangle = 0.85$, and the data shown has different initial temperature values and supersaturation levels provided in the legend of each plot. For MPC, the starting temperature is 13 °C. (a) Protein solute concentration vs time. (b) Crystallizer temperature vs time. (c) Supersaturation vs time.

$$i = 1, 2, \ldots, p \quad \text{and} \quad j \in \{110, 101\} \qquad (29)$$

where Δ is the sampling time, t is the current time, t_i, $i = 1, 2, \ldots, p$, is the time of the ith prediction step, $t_i = t + i\Delta$, t_f is the total simulation time, $F_{\langle \alpha \rangle, i}$ is the cost function penalizing the deviation of the average crystal shape, $\langle \alpha \rangle$, from a desired crystal shape, α_{set}, p is the number of prediction steps, $p\Delta$ is the prediction horizon, and $T_{j,i}$ is the jacket temperature at the ith step, and $T_{j,i} = T_j(t + i\Delta)$. The set of optimal manipulated input values along the prediction

horizon $(T_{j,1}, T_{j,2}, \ldots, T_{j,p})$ is obtained by solving the problem of Eq. (29). The controller is implemented in a receding horizon scheme where the first value of the optimal input trajectory, $T_{j,1}$, is applied to the process until the next sampling time. Then, a new protein concentration measurement is obtained from the kMC simulation, and the MPC problem of Eq. (29) is re-solved by rolling the horizon one step forward.

6. Closed-loop simulations of the batch crystallization process

The proposed model predictive controller solves a constrained minimization problem over a prediction horizon, and computes the optimal jacket temperature, which is then applied to the closed-loop system at each sampling time ($\Delta = 1$ s). Additionally, the uncertainty in the crystallizer is reflected through the random fluctuation in the solute concentration with the Gaussian distribution presented in the following equation:

$$\langle C(t) \rangle = C_n, \quad \langle C(t)C(t') \rangle = \sigma_n^2 C_n^2, \qquad (30)$$

where C_n is the nominal concentration and $\sigma_n C_n$ shows the standard deviation of the concentration measurements. For all closed-loop simulations, the nominal concentration is 47 mg/mL, and the deviation, σ_n, is set to be 1% at pH 4.5 and 4.0% NaCl. The volume of the crystallizer is 5.0 L. Since the MPC makes use of the steady-state growth rates (cf. Fig. 4(b) and (c)), the number of prediction steps is set to be $p = 1$. For the purpose of simulation, the solute concentration fluctuates every 1 s with the nominal value $C_n(t)$ at time t. The closed-loop simulation duration is $t_f = 20,000$ s.

In the closed-loop simulations two desired crystal morphologies, $\langle \alpha \rangle = 1.11$ and $\langle \alpha \rangle = 0.85$, are chosen where these two shapes represent the protein crystal with equidimensional and more elongated length into the (101) direction.

To verify the performance of the proposed MPC, it is compared to those of two other conventional control strategies, CTC and CSC. For further details regarding how CTC and CSC operate, the readers may refer to Kwon et al. (in press). Specifically in Fig. 6, for $\langle \alpha \rangle = 0.85$, the optimal temperature is ~ 24.2 °C, and the nucleation of over 30% of the total crystals occurs within the first 5% of the entire batch run due to the high initial supersaturation level maintained until the system reaches its optimal temperature. We note that the MPC in this case results in a broader crystal shape distribution from a desired set-point value owing to the biased nucleation in the beginning. In spite of this, the simulation under MPC shows a similar crystal shape distribution compared to that of CTC at $T_o = 24.2$ °C where the optimal temperature is maintained for the crystallizer over the entire batch.
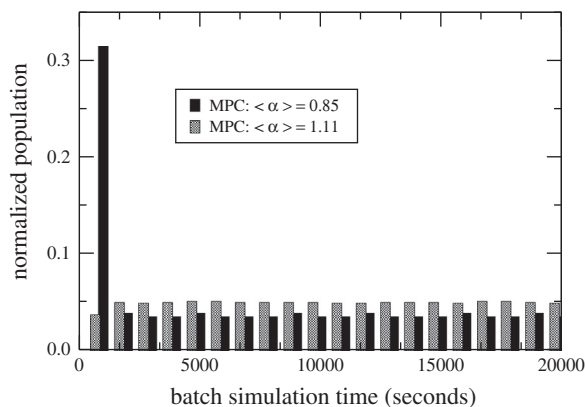

Fig. 6. Normalized nucleation time distribution for the batch run under closed-loop MPC operation for $\langle \alpha \rangle = 0.85$ and $\langle \alpha \rangle = 1.11$, respectively.

The final crystal shape distribution for the MPC in Figs. 7 and 8 can be very narrow and even closer to the desired values when the initial temperature is much closer to the optimal temperature, for example, from $T_o = 13\,°C$ to $T_o = 24.2\,°C$. Furthermore, the controller performance can be further improved by adjusting R_T so that the system is able to change its temperature faster. For further analysis on this, the readers may refer to Liu et al. (2010b).

For the closed-loop simulations at the lower set-point value, $\langle \alpha \rangle = 0.85$, the simulation results are shown in Figs. 5, 7, and 8 for the evolution of the crystallizer temperature, the protein solute concentration, the supersaturation, and the average crystal shape along the batch. Additionally, a snapshot of crystal shape distribution at four different times (5000, 10,000, 15,000, 20,000 s) is presented in Fig. 13. Initially, a simulation under MPC at $c = 47$ mg/mL and $T_o = 13\,°C$ is run. For the initial temperature of the simulations under CTC, two extremes of the temperature profile computed by the simulation under MPC are chosen as follows: $T_o = 13\,°C$ and $T_o = 24.2\,°C$. Similarly, two values for the initial supersaturation of the simulations under CSC are chosen as follows: $\sigma = 2.27$ and $\sigma = 3.40$.

For the lower desired crystal growth rate ratio, $\langle \alpha \rangle = 0.85$, it is recommended to start the crystallizer with a higher initial temperature allowing the system to achieve the optimal temperature earlier in the batch run which will result in a uniform crystal nucleation along the batch run, and the crystals grow under an optimal growth condition from the beginning (Kwon et al., 2013). It is observed in Fig. 5(a) that the simulations under the CSC at $\sigma = 3.4$ and the CTC at $T_o = 13\,°C$ demonstrate the significant depletion in the solute concentration where they both are at high supersaturation levels, and hence high nucleation and growth rates are expected. In contrast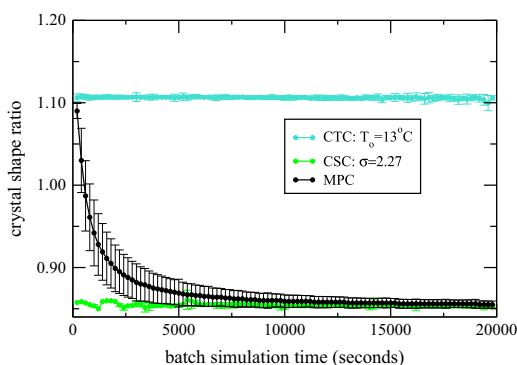, in the proposed MPC, CTC at the high temperature, $T_o = 24.2\,°C$, and the CSC at the low super-saturation, $\sigma = 2.27$, no significant solute concentration drop is observed as a result of the low nucleation and growth rates. For example, in Figs. 5, 7, and 8, the solute concentration, the super-saturation, the temperature, and the average of the shape distribution with time under CTC at $T_o = 13\,°C$ are very similar to those of CSC at $\sigma = 3.40$. Therefore, we note that CTC and CSC policies show similar controller performances when their super-saturation levels are nearly identical over the most part of the batch run. We also note that the proposed MPC with a relatively high initial temperature can outperform other conventional polices, and the performance of the MPC can be by far improved by adjusting the constraint on the rate of change for the jacket temperature.

In Fig. 5(b), the jacket temperature is simply increased to the optimal value by the proposed MPC due to the fact that the solute concentration has minimal depletion. The optimal temperature for the crystal growth of a low growth rate ratio is usually high where the system is especially sensitive to the small changes in the solute concentration and the temperature as it is shown in Fig. 4. The interested reader may refer to our recent work (Kwon et al., 2013) for further analysis on the sensitivity of the controller design in relation to the initial temperature of the crystallizer.

In Table 3, a comparison is shown under different control strategies for the average crystal size along the (110) direction, $\langle h_{110} \rangle$, and r_{10}, r_{50}, r_{90}, which are the 10%, 50%, and 90% population fractions, respectively. For instance, r_{10} for MPC is 3.13 μm, which means that 10% of crystals are smaller than 3.13 μm at the end of the batch run. The span, which is defined as $(r_{90} - r_{10})/r_{50}$, indicates the extent of crystal size distribution. In Table 3 and Figs. 7 and 8, it is demonstrated that the MPC is able to achieve a low polydispersity (a low span value) and a desired crystal shape distribution by appropriately dealing with the undesired effects such as the biased nucleation, disturbances, and the mismatch of moment models. The controller performance can be further improved if we choose an initial temperature sufficiently close to the optimal temperature and use an actuator with higher limitation on the jacket temperature change.

For $\langle \alpha \rangle = 1.11$, a high supersaturation level is favored for a crystal growth with equidimensional shape. As a result, the high nucleation and growth rates result in the significant drop in the solute concentration level. In Fig. 9, it shows that the supersaturation level constantly fluctuates which is attributed to the jacket temperature computed by the proposed MPC. Reflecting the heuristic that the system progresses from metastable to labile regime, the initial rise-and-fall in the supersaturation level can be understood as follows: Initially, the formation of small crystals occurs, and they grow spontaneously. Once a sufficient amount of nucleation occurs, the supersaturation level decreases to a minimum value and it eventually decreases the nucleation rate as well. In the end, the system proceeds to a regime where crystal growth dominates the crystal nucleation. The rise-and-fall in supersaturation, which resulted from the optimal temperature computed by the proposed MPC, extends to the end as the solute concentration steadily decreases from 47 to 40 mg/mL as it

Fig. 7. Profiles of the average of crystal shape distribution with time under CTC and CSC. Additionally MPC is shown using $\langle \alpha \rangle = 0.85$.
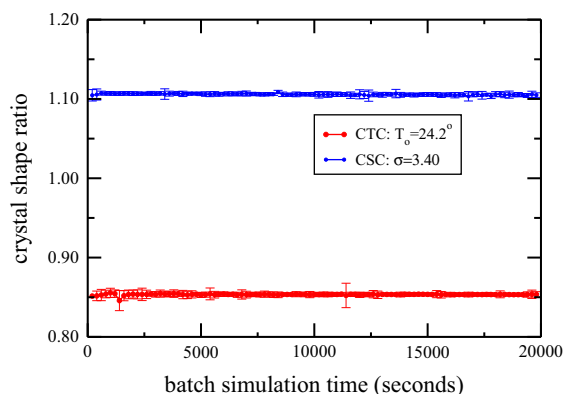

Fig. 8. Profiles of the average of crystal shape distribution with time under CTC and CSC.

Table 3
The simulation results for the crystal size in (110) direction under MPC for $\langle \alpha \rangle = 0.85$, as well as CTC and CSC. Units for the $\langle h_{110} \rangle$, r_{10}, r_{50}, and r_{90} are given in μm.

Control strategy	$\langle h_{110} \rangle$	r_{10}	r_{50}	r_{90}	Span
MPC	26.04	3.13	23.72	48.71	1.91
CTC: T=13 °C	41.27	0.52	3.43	20.94	5.96
CTC: T=24.2 °C	20.11	0.70	18.04	39.20	2.13
CSC: $\sigma = 2.27$	46.06	8.02	41.82	78.73	1.69
CSC: $\sigma = 3.40$	45.33	0.60	2.89	19.25	6.44

is shown in Fig. 9(a)–(c). More specifically, desired crystal nucleation and growth rates, which depend on the supersaturation level, can be regulated by manipulating the temperature and thereby solubility. It is also demonstrated in Fig. 9(b) that the optimal temperature trajectory computed by the proposed MPC does not remain at a constant value as the proposed MPC responds promptly to the solute concentration drop and disturbances in order to avoid the formation of small crystal fines at the end of the batch process. In Fig. 6, since the system reaches the optimal temperature fast, the profile of nucleated crystals with time is uniform throughout the batch run. However, due to the insensitivity of the system to the changes in the supersaturation level at the high supersaturation region, the
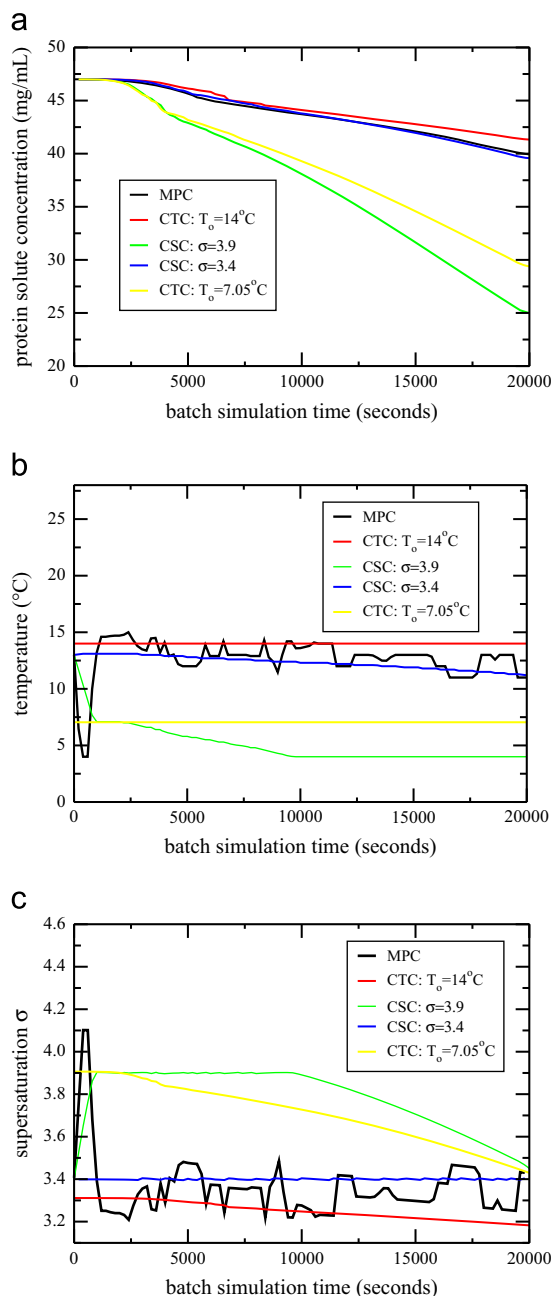
simulation results under other strategies are close to that under MPC, as it is seen in Figs. 10 and 11.

In Table 4, $\langle \alpha \rangle = 1.11$ shows a high polydispersity because of the significant drop in the concentration, but a narrow crystal shape distribution is obtained by a nearly uniform crystal nucleation rate under MPC. The CTC at $T = 14\,°C$ and CSC $\sigma = 3.4$ result in similar shape distributions to that of MPC, but they show high standard deviation in Figs. 10 and 11, and their spans are also high as it is shown in Table 4, which implies that they are not robust when the depletion in the solute concentration is significant.

In Fig. 12, the more equidimensional crystal shape, $\langle \alpha \rangle = 1.11$, can be achieved over a broad supersaturation range, and thus both the proposed MPC and other conventional strategies show good performances in regulating the crystal shape to a desired morphology. However, the conventional control strategies do not guarantee a low polydispersity all the time, because it depends on the growth conditions as it is shown in Table 4. In Fig. 13, it is apparent that the proposed MPC steadily drives the crystal shape distribution to a desired value, and eventually a narrow shape distribution is obtained at the end of the batch run.
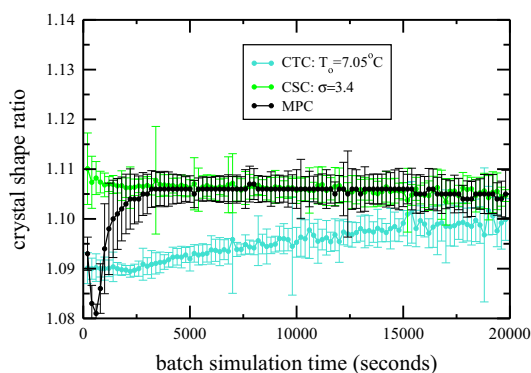

Fig. 10. Profiles of the average of crystal shape distribution with time under CTC and CSC. Additionally MPC is shown using $\langle \alpha \rangle = 1.11$.
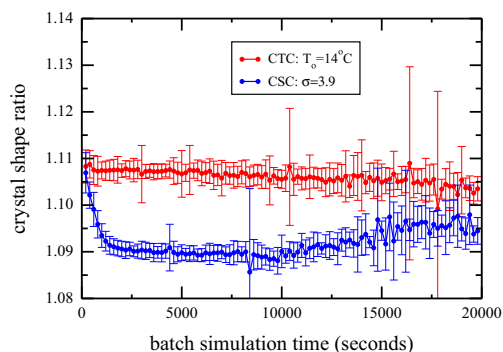

Fig. 11. Profiles of the average of crystal shape distribution with time under CTC and CSC.

Table 4
The simulation results for the crystal size in the (110) direction under MPC for $\langle \alpha \rangle = 1.11$ as well as CTC and CSC. Units for $\langle h_{110} \rangle$, r_{10}, r_{50}, and r_{90} are given in μm.

Control strategy	$\langle h_{110} \rangle$	r_{10}	r_{50}	r_{90}	Span
MPC	31.30	0.49	5.24	14.5	2.67
CTC: $T = 7.05\,°C$	73.61	0.45	1.97	3.84	1.72
CTC: $T = 14\,°C$	23.10	0.74	4.30	17.35	3.87
CSC: $\sigma = 3.4$	33.98	0.93	4.84	20.88	4.12
CSC: $\sigma = 3.9$	88.17	0.41	1.45	3.55	2.16

Fig. 9. Profiles of protein solute concentration, crystallizer temperature, and supersaturation vs. time under closed-loop MPC operation during the batch run. The growth rate ratio set-point value is set at $\langle \alpha \rangle = 1.11$, and the data shown has different initial temperature values and supersaturation levels provided in the legend of each plot. For MPC, the starting temperature is 13 °C. (a) Protein solute concentration vs time. (b) Crystallizer temperature vs time. (c) Supersaturation vs time.
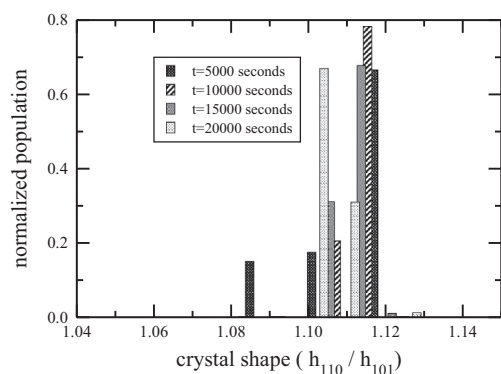
Fig. 12. The normalized crystal shape distribution at four different times during the batch simulation under MPC for $\langle \alpha \rangle = 1.11$.
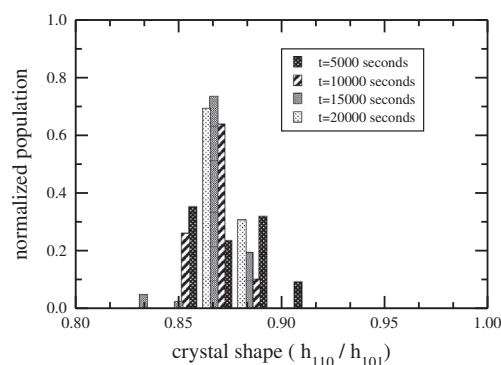

Fig. 13. The normalized crystal shape distribution at four different times during the batch simulation under MPC for $\langle \alpha \rangle = 0.85$.

Fig. 14. The amount of real time necessary to complete the batch crystallization simulations for varying number of cores. The standard error bars represent 1 standard deviation over 10 batch crystallization simulations for each point. The best fit line has equation: time$=1.7492\,(\text{cores})^{-0.65}$ with an $R^2=0.9614$.

In conclusion, MPC can successfully achieve the desired crystal shape distribution and is robust with respect to a biased nucleation and a significant drop in the solute concentration has been demonstrated, however, whether a low polydispersity can be achieved is determined by the desired set-point value. For $\langle \alpha \rangle = 0.85$, crystals with both desired morphology and a low polydispersity can be achieved at a sufficiently high temperature in the crystallizer, where it is typically close to an optimal temperature, because it takes less amount of time for the system to reach its optimal state causing the uniform nucleation to occur throughout the batch. For $\langle \alpha \rangle = 1.11$, however, crystals with a narrow shape distribution and a high polydispersity can be obtained regardless of the initial temperature, because the crystallizer instantly responds to the depletion in the solute concentration, as is shown in Fig. 9. More details regarding robust-control of crystallization systems and model predictive control can be found from Shi et al. (2006), Shi et al. (2005), Chiu and Christofides (2000), and El-Farra et al. (2001).

On a final note, all the batch crystallization simulations executed in this work were done in parallel using Message Passing Interface (MPI) on the Hoffman2 cluster at UCLA. The Hoffman2 cluster is a shared resource which composed of 1032 nodes with a total of 9772 cores. The memory on each node, as well as the CPU speed, varies over the cluster. By using MPI we are able to divide the computational cost and memory requirements over multiple cores. The most computationally expensive part of these simulations is the crystal growth step. Since the crystal growth step is executed independently for each crystal between controller calls, concentration fluctuations, and aggregation events, this step is easily parallelizable. It is also noted that the nucleation process does not affect the crystal growth stage since when a new crystal is born it directly enters the crystal growth process. Fig. 14 shows
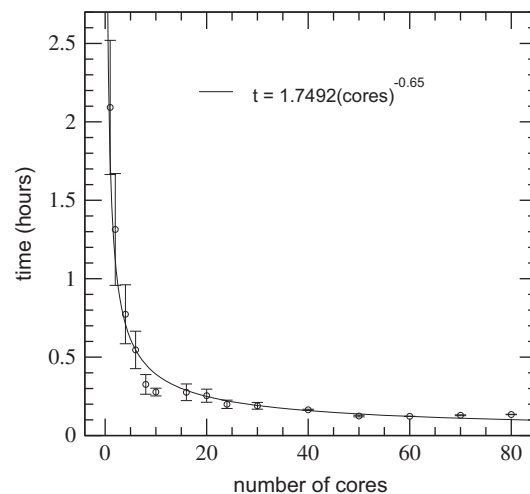
the amount of time necessary to run one batch crystallization simulation depending on the number of cores used. It can also be noticed that since the CPU speed varies, the error bars are quite large for the cases with less CPUs. Through extensive testing we found that using 20 cores was an appropriate tradeoff between time spent sending and receiving messages between cores while still reducing the time spent in the crystal growth process, as well as making sure the scheduler on the Hoffman2 cluster would accept our jobs in a reasonable amount of time. On average the kMC simulations were finished in 0.254 h, spending 46% of the time in the crystal growth process for 20 cores. Due to the fact that all processors do not have the same speed, the process also spent 34% of time waiting for all cores to align in simulation time before controller calls, concentration fluctuations, and aggregation events. When looking at the single core case, 97% of time was spent in the crystal growth process. It is noted that when using more cores, additional overhead is added when trying to balance the number of lysozyme crystals assigned to each core.

7. Conclusions

Initially, the present work focused on the modeling of protein crystal aggregation along with crystal nucleation, and growth in a batch crystallization process via a kinetic Monte Carlo (kMC) simulation. More specifically, the kMC simulation modeled crystal growth via adsorption, desorption, and migration mechanisms on the (110) and (101) faces, and the nucleation rate from the experimental results by Galkin and Vekilov (2001) was used in this work. Then, the aggregation of protein crystals in the batch simulation was modeled through an aggregation kernel accounting for collision efficiency. Having considered the sizes of lysozyme crystals in this study, the aggregation was mainly induced by shear forces. Moreover, binary aggregation was assumed and thus an aggregate was formed as two crystals completely merge along with their internal coordinates. Furthermore, we supposed the crystal shape of the aggregate followed that of the bigger crystal. Additionally, the high-dimensionality in the PBM could lead to a complicated controller design, which could not be immediately implemented in practice. In this end, moment models were derived to describe the dynamic evolution of the three leading moment of crystal volume distribution. Finally, the moment model was used along with a nonlinear algebraic equation and energy and mass balances in order

to design a novel model predictive controller (MPC). Under MPC, the crystal shapes of crystal aggregates were regulated through the manipulation of the jacket temperature measuring the protein solute concentration and the crystallizer temperature which is a common practice in batch crystallization.

Then, the simulation results of the proposed MPC were compared with those of other strategies, CTC and CSC, where these strategies are not robust to a significant concentration drop and the uncertainties in the model. However, the proposed MPC is able to drive the crystal shape distribution to a desired set-point value properly dealing with the biased nucleation and a critical solute concentration drop. Moreover, the production of crystals with a low polydispersity can be achieved depending on the desired crystal shape. For example, for $\langle \alpha \rangle = 1.11$, crystals with a narrow shape distribution are obtained as the MPC promptly counteracts the depletion in the solute concentration. The ability to deal with the undesired effects is reflected as a fluctuation in the optimal crystallizer temperature computed by the proposed MPC as it is shown in Fig. 9, and it leads to an unsteady growth condition which will produce crystals with a relatively high polydispersity.

$$\frac{dM_j}{dt} + G_{volume}\left([V^j n(V,t)]_0^\infty - \int_o^\infty j V^{j-1} n(V,t)\, dV \right)$$
$$= \underbrace{\frac{1}{2}\int_0^\infty V^j \int_0^\infty \alpha_{eff}\beta(V-\overline{V},\overline{V})n(V-\overline{V})n(\overline{V})\,d\overline{V}\,dV - \int_0^\infty V^j n(V)\int_0^\infty \alpha_{eff}\beta(V,\overline{V})n(\overline{V})\,d\overline{V}\,dV}_{aggregation}$$

For $\langle \alpha \rangle = 0.85$, however, crystals with a desired shape distribution and a narrow size distribution can be achieved at a high initial temperature which is close to the optimal temperature, because the unwanted biased nucleation can be properly avoided. Additionally, allowing for a faster jacket temperature (manipulated input) change can be another choice reducing the amount of time needed to obtain crystals with desired properties, because the state of system reaches its optimal value faster.

Appendix A. Derivation of the boundary condition for PBM

As is pointed out by Miller (1993), Eq. (17) can be rewritten by replacing the nucleation term with an appropriate boundary condition. Integrating Eq. (17) over V from 0^- to 0^+ gives

$$G_{volume}\int_{0^-}^{0^+}\frac{\partial n(V,t)}{\partial V}\,dV = B(T,c),$$

since

$$\int_{0^-}^{0^+} B(T,c)\delta(V)\,dV = B(T,c),$$

and

$$\int_{0^-}^{0^+}\frac{\partial n(V,t)}{\partial t}\,dV = 0.$$

Additionally, when the average crystal volume is very small (i.e., $V \simeq 0$), the aggregation rarely occurs and thus it is assumed

that the aggregation terms are negligible:

$$\frac{1}{2}\int_{0^-}^{0^+}\int_0^V \beta(V-\overline{V},\overline{V})n(V-\overline{V})n(\overline{V})\,d\overline{V}\,dV$$
$$= \int_{0^-}^{0^+} n(V)\int_0^\infty \beta(V,\overline{V})n(\overline{V})\,d\overline{V}\,dV = 0$$

and

$$n(V,t) = 0 \quad \text{at } V = 0^-, \quad n(V,t) = n(0,t) \quad \text{at } V = 0^+,$$

assuming all nuclei form with size $V=0$. Then, Eq. (17) can be reduced to the following:

$$G_{volume}n(0,t) = B(T,c) \quad \text{at } V = 0.$$

Appendix B. Derivation of the first moment model

We multiply the jth power of the crystal volume V^j on both sides of Eq. (19), and integrate them from $V=0$ to $V=\infty$, to obtain

Suppose that $n(V,t)$ is finite at $V=0$ and $n(V,t) \to 0$ as $V \to \infty$. This implies that there are a finite number of nucleated crystals with infinitesimal volume but there are no crystals with infinite size at time t. Since the total crystal volume is independent of the aggregation rate and depends only on the nucleation rate, the right hand side in the equation above, which is denoted as "aggregation", simply does not contribute to the first moment equation that describes the evolution of M_1 with time. As an example, the derivation of the first moment model is presented in more detail.

First moment: Making the substitution $V-\overline{V}=y$ and thus $dV=dy$ on the right hand side of the equation above, and using that $M_1 = \int_o^\infty V n(V,t)\,dV$, we obtain

$$\frac{dM_1}{dt} - G_{volume}M_0$$
$$= \frac{1}{2}\int_0^\infty V\left[\int_0^\infty \alpha_{eff}\beta(y,\overline{V})n(\overline{V},t)\,d\overline{V}\right]n(y,t)\,dy$$
$$\quad - \int_0^\infty V\left[\int_0^\infty \alpha_{eff}\beta(V,\overline{V})n(\overline{V},t)\,d\overline{V}\right]n(V,t)\,dV$$
$$= \frac{1}{2}\int_0^\infty (\overline{V}+y)\left[\int_0^\infty \alpha_{eff}(\overline{V}^{1/3}+y^{1/3})^3 n(\overline{V},t)\,d\overline{V}\right]n(y,t)\,dy$$
$$\quad - \int_0^\infty V\left[\int_0^\infty \alpha_{eff}(V^{1/3}+\overline{V}^{1/3})^3 n(\overline{V},t)\,d\overline{V}\right]n(V,t)\,dV$$
$$= \frac{\alpha_{eff}}{2}[8M_1 M_3 + 6M_2^2 + 2M_0 M_4] - \alpha_{eff}[M_0 M_4 + 4M_1 M_3 + 3M_2^2] = 0$$

References

Aldabaibeh, N., Jones, M.J., Myerson, A.S., Ulrich, J., 2009. The solubility of orthorhombic lysozyme chloride crystals obtained at high pH. Crystal Growth and Design 9, 3313–3317.

Balakin, B., Hoffmann, A.C., Kosinski, P., 2012. The collision efficiency in a shear flow. Chemical Engineering Science 68, 305–312.

Bortz, A.B., Kalos, M.H., Lebowitz, J.L., 1975. New algorithm for Monte Carlo simulation of Ising spin systems. Journal of Computational Physics 17, 10–18.

Cacioppo, E., Munson, S., Pusey, M.L., 1991. Protein solubilities determined by a rapid technique and modification of that technique to a micro-method. Journal of Crystal Growth 110, 66–71.

Cacioppo, E., Pusey, M.L., 1991. The solubility of the tetragonal form of hen egg white lysozyme from pH 4.0 to 5.4. Journal of Crystal Growth 114, 286–292.

Camp, T.R., Stein, P.C., 1943. Velocity gradients and internal work in fluid motion. Journal of the Boston Society of Civil Engineers 30, 219–237.

Cheng, J., Yang, C., Mao, Z., Zhao, C., 2009. CFD modeling of nucleation, growth, aggregation, and breakage in continuous precipitation of barium sulfate in a stirred tank. Industrial and Engineering Chemistry Research 48, 6992–7003.

Chiu, T., Christofides, P.D., 1999. Nonlinear control of particulate processes. AIChE Journal 45, 1279–1297.

Chiu, T., Christofides, P.D., 2000. Robust control of particulate processes using uncertain population balances. AIChE Journal 46, 266–280.

Christofides, P.D., Armaou, A., Lou, Y., Varshney, A., 2008. Control and Optimization of Multiscale Process Systems. Birkhäuser, Boston.

Dai, J., Kanter, J.M., Kapur, S.S., Seider, W.D., Sinno, T., 2005. On-lattice kinetic Monte Carlo simulations of point defect aggregation in entropically influenced crystalline systems. Physical Review B 72, 134102.

Dai, J., Seider, W.D., Sinno, T., 2008. Coarse-grained lattice kinetic Monte Carlo simulation of systems of strongly interacting particles. Journal of Chemical Physics 128, 194705.

Durbin, S.D., Feher, G., 1986. Crystal growth studies of lysozyme as a model for protein crystallization. Journal of Crystal Growth 76, 583–592.

Durbin, S.D., Feher, G., 1991. Simulation of lysozyme crystal growth by the Monte Carlo method. Journal of Crystal Growth 110, 41–51.

El-Farra, N.H., Chiu, T., Christofides, P.D., 2001. Analysis and control of particulate processes with input constraints. AIChE Journal 47, 1849–1865.

Feher, G., Kam, Z., 1985. Nucleation and growth of protein crystals: general principles and assays. Methods in Enzymology 114, 77–112.

Fichthorn, K.A., Weinberg, W.H., 1991. Theoretical foundations of dynamical Monte Carlo simulations. Journal of Chemical Physics 95, 1090–1096.

Forsythe, E.L., Nadarajah, A., Pusey, M.L., 1999. Growth of (101) faces of tetragonal lysozyme crystals: measured growth-rate trends. Acta Crystallographica Section D 55, 1005–1011.

Galkin, O., Vekilov, P.G., 1999. Direct determination of the nucleation rates of protein crystals. Journal of Physical Chemistry B 103, 10965–10971.

Galkin, O., Vekilov, P.G., 2001. Nucleation of protein crystals: critical nuclei, phase behavior, and control pathways. Journal of Crystal Growth 232, 63–76.

Gillespie, D.T., 1976. A general method for numerically simulating the stochastic time evolution of coupled chemical reactions. Journal of Computational Physics 22, 403–434.

Gillespie, D.T., 2007. Stochastic simulation of chemical kinetics. Annual Review of Physical Chemistry 58, 35–55.

Gilmer, G.H., Bennema, P., 1972. Simulation of crystal growth with surface diffusion. Journal of Applied Physics 43, 1347.

Henzler, H., 2000. Particle stress in bioreactors. Advances in Biochemical Engineering/Biotechnology 67, 35–82.

Hollander, E.D., Derksen, J.J., Kramer, H.M.J., Van Rosmalen, G.M., Van den Akker, H. E.A., 2003. A numerical study on orthokinetic agglomeration in stirred tanks. Powder technology 130, 169–173.

Ilievski, D., Livk, I., 2006. An agglomeration efficiency model for gibbsite precipitation in a turbulently stirred vessel. Chemical Engineering Science 61, 2010–2022.

Jiang, Q., Logan, B.E., 1991. Fractal dimensions of aggregates determined from steady-state size distributions. Environmental Science and Technology 25, 2031–2038.

Kalani, A., Christofides, P.D., 2002. Simulation, estimation and control of size distribution in aerosol processes with simultaneous reaction, nucleation, condensation and coagulation. Computers and Chemical Engineering 26, 1153–1169.

Ke, S.C., DeLucas, L.J., Harrison, J.G., 1998. Computer simulation of protein crystal growth using aggregates as the growth unit. Journal of Physics D: Applied Physics 31, 1064–1070.

Kurihara, K., Miyashita, S., Sazaki, G., Nakada, T., Suzuki, Y., Komatsu, H., 1996. Interferometric study on the crystal growth of tetragonal lysozyme crystal. Journal of Crystal Growth 166, 904–908.

Kusters, K.A., Wijers, J.D., Thoenes, D., 1997. Aggregation kinetics of small particles in agitated vessels. Chemical Engineering Science 52, 107–121.

Kwon, J.S., Nayhouse, M., Christofides, P.D., Orkoulas, G., 2013. Modeling and control of protein crystal shape and size in batch crystallization. AIChE Journal 59, 2317–2327.

Kwon, J.S., Nayhouse, M., Christofides, P.D., Orkoulas, G. Protein crystal shape and size control in batch crystallization: comparing model predictive control with

conventional operating policies. Industrial and Engineering Chemistry Research, http://dx.doi.org/ 10.1021/ie400584g, in press.

Liang, M., Jin, F., Liu, R., Yu, Y., Su, R., Wang, L., Qi, W., He, Z., 2013. Shape evolution and thermal stability of lysozyme crystals: effect of pH and temperature. Bioprocess and Biosystems Engineering 36, 91–99.

Liu, J.J., Ma, C.Y., Hu, Y.D., Wang, X.Z., 2010a. Effect of seed loading and cooling rate on crystal size and shape distributions in protein crystallization—a study using morphological population balance simulation. Computers and Chemical Engineering 34, 1945–1952.

Liu, J.J., Ma, C.Y., Hu, Y.D., Wang, X.Z., 2010b. Modelling protein crystallisation using morphological population balance models. Chemical Engineering Research and Design 88, 437–446.

Miller, S.M., 1993. Modelling and Quality Control Strategies for Batch Cooling Crystallizers. Ph.D. Thesis, The University of Texas at Austin.

Müller, C., Liu, Y., Migge, A., Pietzsch, M., Ulrich, J., 2011. Recombinant L-asparaginase B and its crystallization—what is the nature of protein crystals? Chemical Engineering and Technology 34, 571–577.

Müller, C., Ulrich, J., 2011. A more clear insight of the lysozyme crystal composition. Crystal Research and Technology 46, 646–650.

Müller-Krumbhaar, H., Binder, K., 1973. Dynamic properties of the Monte Carlo method in statistical mechanics. Journal of Statistical Physics 8, 1–24.

Nanev, C.N., Tsekova, D., 2000. Heterogeneous nucleation of hen-egg-white lysozyme-molecular approach. Crystal Research and Technology 35, 189–195.

Nayhouse, M., Kwon, J.S., Christofides, P.D., Orkoulas, G., 2013. Crystal shape modeling and control in protein crystal growth. Chemical Engineering Science 87, 216–223.

Pusey, M.L., Nadarajah, A., 2002. A model for tetragonal lysozyme crystal nucleation and growth. Crystal Growth and Design 2, 475–483.

Rathinam, M., Petzold, L.R., Cao, Y., Gillespie, D.T., 2003. Stiffness in stochastic chemically reacting systems: the implicit tau-leaping method. Journal of Chemical Physics 119, 12784–12794.

Reese, J.S., Raimondeau, S., Vlachos, D.G., 2001. Monte Carlo algorithms for complex surface reaction mechanisms: efficiency and accuracy. Journal of Computational Physics 173, 302–321.

Rosenberger, F., Vekilov, P.G., Muschol, M., Thomas, B.R., 1996. Nucleation and crystallization of globular proteins—what we know and what is missing. Journal of Crystal Growth 168, 1–27.

Saffman, P.G., Turner, J.S., 1954. On the collision of drops in turbulent clouds. Journal of Fluid Mechanics 1, 448–462.

Schmidt, S., Havekost, D., Kaiser, K., Henzler, H.K., 2005. Crystallization for the downstream processing of proteins. Engineering in Life Sciences 5, 273–276.

Shi, D., El-Farra, N.H., Li, M., Mhaskar, P., Christofides, P.D., 2006. Predictive control of particle size distribution in particulate processes. Chemical Engineering Science 61, 268–281.

Shi, D., Mhaskar, P., El-Farra, N.H., Christofides, P.D., 2005. Predictive control of crystal size distribution in protein crystallization. Nanotechnology 16, S562–S574.

Smejkal, B., Helk, B., Rondeau, J., Anton, S., Wilke, A., Scheyerer, P., Fries, J., Hekmat, D., Weuster-Botz, D., 2013. Protein crystallization in stirred systems-scale-up via the maximum local energy dissipation. Biotechnology and Bioengineering 110, 1956–1963.

Snyder, M.A., Chatterjee, A., Vlachos, D.G., 2005. Net-event kinetic Monte Carlo for overcoming stiffness in spatially homogeneous and distributed systems. Computers and Chemical Engineering 29, 701–712.

Suzuki, Y., Miyashita, S., Komatsu, H., Sato, K., Yagi, T., 1994. Crystal growth of hen egg white lysozyme under high pressure. Japanese Journal of Applied Physics 33, 1568–1570.

Vanni, M., Baldi, G., 2002. Coagulation efficiency of colloidal particles in shear flow. Advances in Colloid and Interface Science 97, 151–177.

Vekilov, P.G., Chernov, A.A., 2003. The physics of protein crystallization. Solid State Physics 57, 1–147.

Wang, L., Lee, M.H., Barton, J., Hughes, L., Odom, T.W., 2008. Shape-control of protein crystals in patterned microwells. Journal of the American Chemical Society 130, 2142–2143.

Wang, L., Marchisio, D.L., Vigil, R.D., Fox, R.O., 2005. CFD simulation of aggregation and breakage processes in laminar Taylor–Couette flow. Journal of Colloid and Interface Science 282, 380–396.

Weber, M., Jones, M., Ulrich, J., 2008. Crystallization as a purification method for jack bean urease: on the suitability of poly(ethylene), Li$_2$SO$_4$ and NaCl as precipitants. Crystal Growth and Design 8, 711–716.

Wiencek, J.M., 1999. New strategies for protein crystal growth. Annual Review of Biomedical Engineering 1, 505–534.